Performances of a resistive Micromegas module for the Time Projection Chambers of the T2K Near Detector upgrade

Abstract

Keywords:

Contents

1. Introduction

T2K [1] is a long-baseline neutrino oscillation experiment exploiting a muon neutrino beam produced by the JPARC accelerator complex in Japan. The T2K experiment includes the beamline, a set of near detectors (INGRID and ND280) and the far detector SuperKamiokande.

T2K provided the first evidence of non-zero mixing angle θ_{13} [2] and discovered the appearance of electron neutrinos in a muon neutrino beam [2, 3, 4]. Combining T2K data with precise θ_{13} measurement from reactor experiments, T2K has recently reported hints of large Charge-Parity (CP) violation in the leptonic sector [5], excluding CP-conservation at about 2σ Confidence Level.

The T2K collaboration is now preparing the second phase of the experiment (T2K-II), starting in Fall 2022, which will exploit the upgrade of the beam from 500 kW to 750 kW. T2K-II will collect in total more than 10^{22} Protons-On-Target (POT), including the 3.6×10^{21} POT already collected, thus enabling 3σ sensitivity on CP-Violation, in case of maximally violated CP. In order to cope with such increased statistics, an improved control of the systematic uncertainty is needed. To this aim, an upgrade of ND280 is being constructed.

ND280 is a magnetized multi-purpose detector that measures the neutrino differential rate before the oscillation, constraining neutrino flux and neutrino-nucleus interaction cross-section. The present ND280 consists of two main parts: an upstream π^0 detector (P0D) and a downstream tracker including two Fine Grained Scintillators (FGD) interleaved with three vertical Time Projection Chambers (TPCs). The P0D and the tracker are surrounded by an electromagnetic calorimeter (ECAL) and by the UA1 magnet providing a 0.2 T magnetic field. The magnet yoke is further instrumented with a Side Muon Range Detector (SMRD).

The role of ND280 in the T2K oscillation analysis is crucial, allowing to constrain the uncertainty on the expected number of events at the far detector down to 4-5%. ND280 measurements are performed on different targets (Carbon and Oxygen) and rely on the precise measurement of the muon momentum measured by the TPCs, with a momentum resolution of 10% at 1 GeV [6]. Better resolution is not needed since the determination of the neutrino energy from the muon momentum is limited by the smearing induced by the Fermi momentum of the nucleus.

Another important result of ND280 is the measurement of the ν_e con-

tamination in the beam [**?**], that constitutes the main background to the ν_e appearance in the electron-like sample selected at Super-Kamiokande. This analysis, based on the Particle Identification (PID) capabilities of the TPCs and of ECAL, is possible thanks to the deposited energy resolution of 8% in the TPCs that allow sufficient e-μ separation between few hundreds MeV and $\sim$2 GeV.

The upgrade of ND280 consists in substituting the P0D with a new tracker, similar to the existent one but with an horizontal geometry. The new tracker includes a 3-dimensional scintillator (Super-FGD) made of about 2 million of 1 cm^3 cubes, read out by wavelength shifting fibers in the 3 directions. On the top and the bottom of the Super-FGD, two TPCs (High-Angle TPCs) will be installed. The new tracker system will be surrounded by six Time-of-Flight modules. This new detector configuration will allow to improve the angular acceptance of ND280, being close to the full 4π phase-space accessible at SuperKamiokande. In addition, the better tracking performances of the super-FGD will allow to improve the reconstruction of the hadronic part of the neutrino interactions, that will be exploited in combination with the muon kinematics.

Each endplate of the new TPCs will be instrumented with eight Micromegas type charge readout modules. The Micromegas detector charge amplification structure uses a resistive anode to spread the charges over several pads to improve the space point resolution. This innovative technique is combined with the bulk-Micromegas technology [6] to compose the "Encapsulated Resistive Anode Micromegas" (ERAM) detector. Performances of a prototype of an ERAM detector exposed to a test beam at CERN were shown in [7]. This paper describes the performance of one ERAM module, built with the same design that will be used for the HA-TPCs, exposed to an electron beam at DESY. With respect to [7], in this paper we characterize both, spatial and dE/dx resolution as a function of the angle of the track with respect to the ERAM plane.

The HA-TPC should fulfill similar performances of existing TPCs in terms of momentum and dE/dx resolution. In addition, the super-FGD will enable the reconstruction of low momentum protons and neutrons [8], thus allowing to reconstruct the neutrino energy more precisely and *effectively* correct for the Fermi momentum: an improved track momentum resolution in HA-TPC, even beyond the previous specifications, is therefore useful to improve the neutrino energy resolution and, ultimately, the precision on neutrino oscillation measurements.

2. Resistive Micromegas

The ERAM detector uses the bulk-Micromegas technology invented in 2004 by a collaboration between CERN/EP-DT-EF PCB workshop and CEA-IRFU [9]. It was developed and used for the construction of the 72 bulk-Micromegas modules (9 m^2 total area) which equip the three T2K/ND280 vertical TPCs. The woven micromesh of the Micromegas detector is sandwiched between two layers of the same insulating material (pyralux) and exposed to UV radiation at the location where the pyralux is kept on top of the pad-segmented anode PCB after chemical development.

The ERAM detector is a 128 μm amplification gap bulk-Micromegas using the standard SD45/18 304L woven micromesh built on top of a resistive anode PCB. When a track crosses the gas volume of a TPC, it generates a cloud of ionized electrons. These electrons are drifted to the anode readout plane of the TPC under a uniform electric field. On the readout plane an avalanche is generated by an high electric field in the Micromegas amplification region. The 3D position of the track is then reconstructed from the arrival time and the position of the avalanche on the readout plane. In the case of the bulk-Micromegas, the electron avalanche in the amplification gap is quite narrow w.r.t the pad size and therefore the position resolution is often limited by the pad size. The resistive anode Micromegas, first introduced and extensively studied by the ILC-TPC collaboration [10], provides a way to induce a signal on a larger number of pads allowing for a better reconstruction of the track position. The sketch of the bulk and the resistive Micromegas concepts are presented in Figure 1.

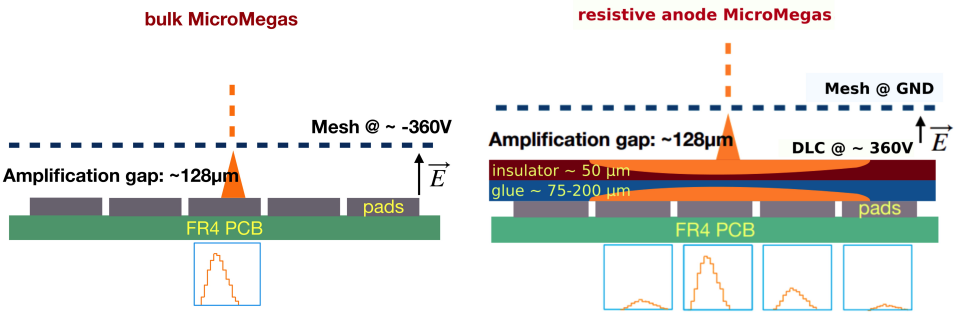

Figure 1: Sketch of Standard Bulk Micromegas layout (left) and Resistive anode Micromegas layout (right).

The anode, segmented in pads, is covered by a foil of insulating material, which has a thin resistive layer on its top side. The ERAM detector uses a Diamond-Like Carbon (DLC) thin layer sputtered on a 50 μm thick APICAL (Kapton) insulator sheet. The avalanche is then naturally quenched because the potential difference locally drops in presence of a high charge density. The resistive layer acts like a 2-D RC network and the charge deposited by the avalanche spreads naturally with time with a Gaussian behaviour. For a point charge deposited at $r = 0$ and $t = 0$, the charge density as a function of radius r and time t is given by:

$$\rho(r,t) = \frac{RC}{4\pi t} e^{\frac{-r^2 RC}{4t}} \tag{1}$$

where R is the resistivity per unit area and C the capacitance per unit area. For this structure, the capacitance C is defined by the distance between the resistive layer and the grounded pads (glue thickness plus APICAL foil). The insulating layer thickness determines the amount of spreading and the charge spread σ_t of the charge collected and integrated by a front-end electronics of shaping time t is given by $\sigma_t = \sqrt{\frac{2t}{RC}}$.

The resistive anode provides mainly two advantages: by spreading the charge between neighbouring pads, it improves greatly the resolution with respect to the pitch/$\sqrt{(12)}$ provided by a mere hodoscope, and it suppresses the formation of sparks and limits their intensity. A further and novel improvement of this technique is a new High Voltage powering scheme, where the mesh is set to ground and the anode to a positive amplification voltage. The insulation of the resistive anode from the pads, hence from the electronics, ensures a a safe operation by a capacitive coupling readout and thus allows us to get rid of the cumbersome anti-spark protection circuitry necessary in the case of the standard bulk readout.

At the end of 2017, a first series of prototypes were produced and tested to assess the feasibility of large charge spreading by a low resistivity anode. The vertical TPCs PCB, with an active area of 36×34 cm^2 covered by 0.97×0.69 cm^2 pads, was adapted to build an ERAM structure with "on-shelf" 2.5 MOhm/$\square$ DLC foils. This first prototype was tested with particle beam at CERN in 2018 and its performance are summarized in [7].

In fall 2018, the global design of the ND280 upgrade detector was fixed. The sub-detector envelops were defined and the size of the ERAM modules fixed to be 420×340 mm^2 with 32×36 rectangular pads of size 10.09×11.18

mm^2. The ERAM module studied in this paper has a resitivity close to the required one of 200 kOhm/$\square$ using DLC foils stack on a 75 μm glue layer. The resistivity maps measured at critical steps of the manufacturing of the DLC foil shows a non uniformity of 20%. The detector is readout with two analog 576 channels AFTER based Front-End Cards (eight 72 channels AFTER ASIC per card). This prototype was tested in a beam test at DESY in June 2019.

3. Experimental setup

The prototype has been exposed to an electron beam at the DESY II test beam facility [11]. DESY II provides electron beams of $1 - 6$ GeV/c at a rate of up to several kHz, depending on the chosen momentum. In the test beam area TB24/1, a large-bore superconducting solenoid, called PCMAG, provides a magnetic field of up to 1.25 tesla. The magnet is mounted on a movable platform, which allows the setup to be moved horizontally and vertically, perpendicular to the beam line, as well as rotated by $\pm 45^\circ$ in the horizontal plane. The platform can position the device under test with a precision of about 0.2 mm horizontally, 0.1 mm vertically, and within 0.1° in angle.

Inside the bore of the magnet, a rail system is installed on which test devices can be mounted at different positions within the magnet. The TPC prototype is supported on a sled, which can move in and out of the magnet and can be used to rotate the chamber around the magnetic field axis as illustrated in Figure 2.

Usually the magnet is positioned perpendicular to the beam. The walls of the magnet present about 20 % of a radiation length, so that an electron beam of 6 GeV/c easily penetrates the magnet and the device under test. A set of four consecutive scintillation counters, of which each has an area of approximately 2.5 cm $\times$ 2.5 cm, is mounted about 1.5 m in front of the magnet. The coincidence between them is used as a beam trigger. In addition, a second set of scintillation counters above and below the magnet provides a cosmic trigger for tests without beam.

The prototype has been placed inside the 0.2 T PCMAG magnet and has been operated for these measurements with a gas mixture of 95% argon, 3% tetrafluoromethane (CF_4), and 2% isobutane (iC_4H_{10}). The gas quality was constantly monitored during the measurement. For the results reported in this paper, the oxygen contamination was around 30 ppm at a gas flow rate

of 30 ℓ/h. The chamber was operated at atmospheric pressure. Ambient temperature and pressure were constantly monitored.

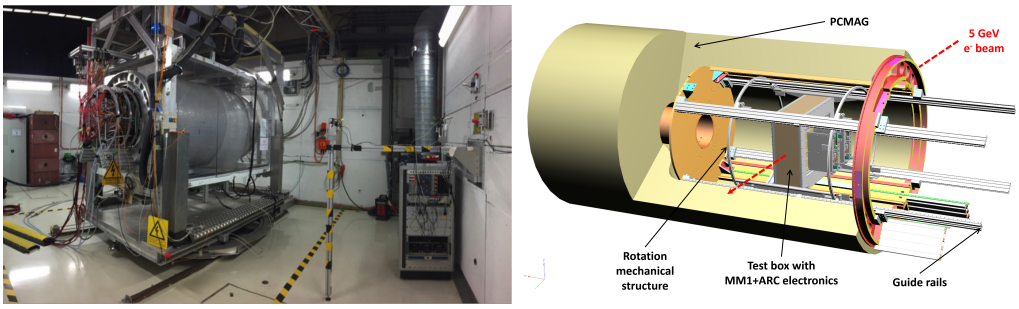

Figure 2: View of the setup.

4. Collected data

The collected data is used to analyze in detail the role of all the relevant parameters (peaking time, DLC voltage, drift distance), to fully characterize the charge spreading, the resistive foil uniformity and to ensure a performance satisfying the ND280 upgrade requirements. The tests at DESY have been done in a short chamber of 15 cm drift distance. The prototype was operated at a voltage of 360 V. The settings chosen for the AFTER chip were a sampling time of 40 ns, a peaking time of 412 ns or 200 ns and a gain of 120 fC.

The results presented in this paper were obtained with electrons with momenta varying from 0.5 to 5 GeV/c. We have carried out drift distance scans with seven points, spaced by 2 cm, at $B = 0T$ and $B = 0.2\ T$, peaking time of 200 ns or 412 ns and high voltage of 370 V and 360 V. In addition a scan of the DLC voltage, varied from 330 V to 400 V, was performed.

We have calibrated the $T0$, the moving table position, and the drift velocities at different drift fields with a 4 GeV/c electron beam and a short peaking time of 116 ns. At the standard T2K field of 275 V/cm, we obtained $V_{\text{drift}} = 7.68\text{cm}/\mu s$ by drift distance scans with the accelerator beam. A Gas Monitoring Chamber (GMC), identical to the ones deployed at T2K's ND280 detector [6], monitored the exhaust gas for the duration of the beam-time. The GMC measured a drift velocity of $7.81 \pm 0.02\text{cm}/\mu s$ at the T2K field, in agreement with the beam scans, see Figure 3. Under the electric field of 140 V/cm, which is associated with the minimum transverse diffusion, we found

a drift velocity of 5.84cm/μs. Despite the impact of the gas bottle changes, the drift velocity V_{drift} under the electric field of $E = 275\text{V/cm}$ varies less than 6‰.

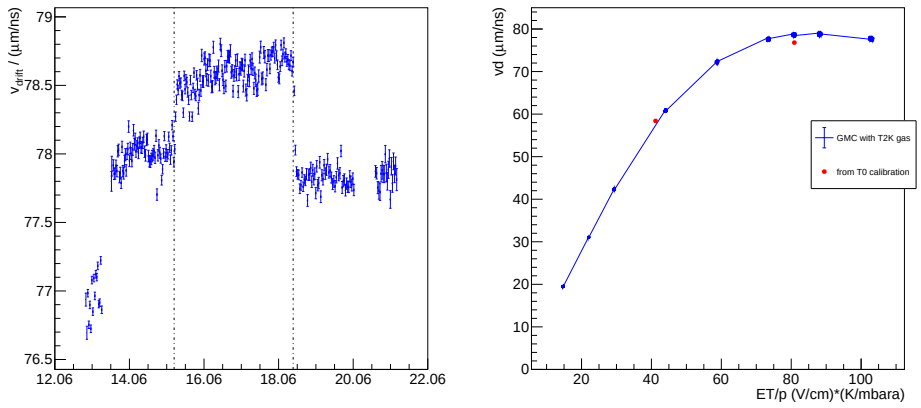

a b

Figure 3: The drift velocity under a constant field of 275 V/cm (a) and as a function of electric field (b) with density corrections applied. The vertical lines on (a) correspond where the bottles of premixed gas were swapped. Transition regions at ramp-up and between bottle changes can clearly be seen. The measurements at different fields in (b) correspond to a full day during the first bottle (14.06).

5. Characterisation of the charge spreading

As explained before, the resistive Micromegas technology produces a spreading of the collected charge into neighboring pads. The charge spreading phenomenon, which drives the waveform shape, is described in [10]. The signal induced by resistive layer is smaller in amplitude and longer in time comparing to the direct charge deposition from the track in the leading pad as illustrated in Figure 5. Hence, the charge spreading is significant in the transverse direction w.r.t. the track while in the longitudinal direction, it's masked by the direct charge. To study the phenomenon of interest, we define a "cluster" as a group of pads in the perpendicular direction to the track. The schematic view of such a cluster for horizontal track and a waveforms in adjacent pads are shown in Figure 4.

In Figure 5, the pad multiplicity per cluster and the fraction of charge in the pad with largest signal ($q_{\text{max}}/q_{\text{cluster}}$) are shown. Most of the clusters

are formed by more than two pads and the pad with largest signal contains typically 80% of the total collected charge. The effect of the high voltage on the multiplicity is also clearly seen in Figure 5. The cluster multiplicity increases with the high voltage.

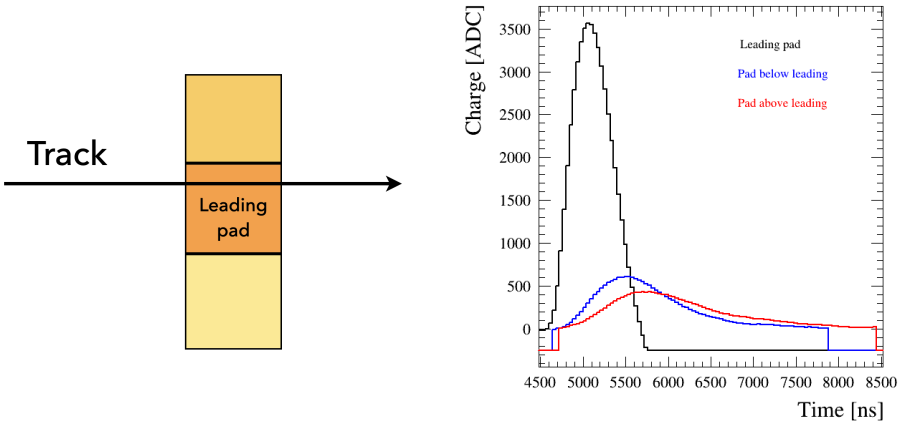

Figure 4: A schematic view of a column cluster (left) and the waveforms of each pad composing this cluster (right) for 412 ns shaping time.

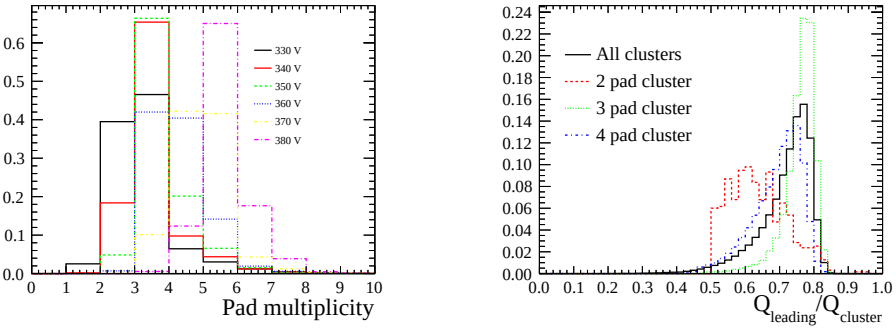

Figure 5: The number of pads in a cluster versus the high voltage (left) and the fraction of the cluster charge which is collected in the pad with largest signal with 360 V (right).

For tracks parallel to the pad plane, transverse spreading is defined precisely within the given column. While for oblique tracks and large square pads, the separation between longitudinal and transverse spreading is more

complicated. In order to distinguish these two spreading topologies, we define more sophisticated cluster patterns shown on Figure 6. These clusters are repeated to pave the whole ERAM. In the case of square pads, these patterns are optimized for angles with tangents 0, 1, 0.5, 0.3 respectively. In the case of rectangular pads, the optimal angles are slightly different.

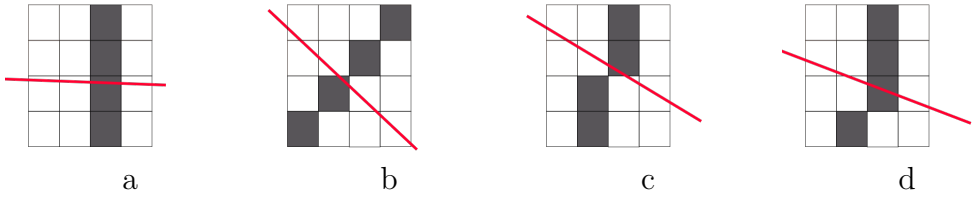

Figure 6: The different cluster patterns that can be used depending on the track angle (red line): (a) column, (b) diagonal, (c) 2 by 1, (d) 3 by 1.

6. Track reconstruction

In the beam test analysis, we focus on the studies of the through-going tracks as more complicated typologies (e.g. showering, curved low-energy tracks) can bias the results. Hence simple reconstruction algorithms DBSCAN [12] are sufficient in our case.

We select a track if it is crossing the whole detector without breaks or splits. A split is defined as the case where there is more than one cluster in a given column. An event containing a split is thus a multiple track event which is dismissed. However, with the resistive spreading, two parallel tracks may not be separated with a gap and thus misreconstructed as one single track. To reject such a topology, a cut on the pad multiplicity in each cluster was implemented. The cut value was optimised for each MicroMegas voltage and electronics shaping time. Examples of the accepted and dismissed events are shown in Figure 7 (a) and (b) respectively.

7. Spatial resolution

As described in section 1, the momentum resolution has to be better than 10% at 1 GeV/c but, to fully exploit the ND280 upgrade capabilities, an even better momentum resolution would be suitable. The momentum resolution is directly connected to the spatial resolution through the Gluckstern

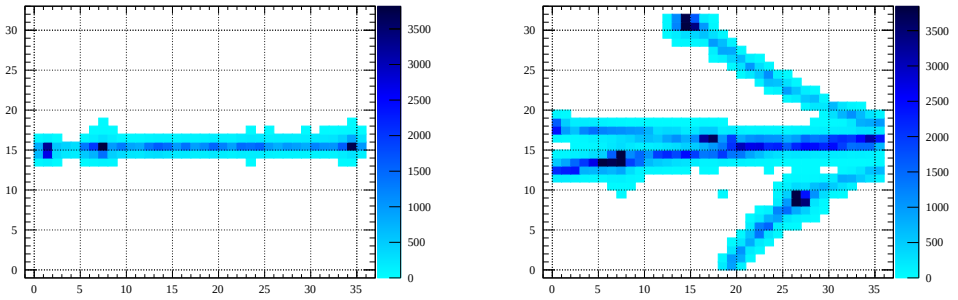

a b

Figure 7: Event displays of the (a) single track and (b) multi-track in the prototype.

formula [13]. For tracks with 70 point measurements, a maximum drift distance of 1 m, and a magnetic field of 0.2 T, a spatial resolution of $\sim 800\mu m$ would be sufficient to reach a momentum resolution of 10% at 1 GeV/c.

As we will show in this section, the resistive Micromegas technology allows to sensibly improve the spatial resolution with respect to the bulk Micromegas, even in presence of slightly larger pads thus allowing to reduce by $\sim 30\%$ the total number of channels for the same active surface. The test beam data have been used to characterize the ERAM module performances for electrons with different angles.

7.1. The Pad Response Function method

The charge spread described in the section 5 results in charge detection in a few pads around the avalanche arrival point. The charge measurements are discrete with the finite pad size, while the spreading in the RC layer is continuous. Thus the barycentric method (Center of Charge, weighted mean) that assigns all the collected charge to the pad center doesn't provide a precise position reconstruction. Instead, we used the so-called Pad Response Function (PRF) which characterizes the relation between observed charge ratios and track position w.r.t. the pad (Equation 2). This method improves the spatial resolution compared to the barycentric method for TPCs with the resistive anode [14]. The PRF is defined as:

$$PRF(x_{track} - x_{pad}) = Q_{pad}/Q_{cluster} \tag{2}$$

where x_{track} is the reconstructed position of the track, x_{pad} is the center of the pad, Q_{pad} is the charge collected on a given pad and $Q_{cluster}$ is the charge collected on the whole cluster. The definition of the cluster is the same as described in section 5. It's a group of pads where one receives a charge from the initial avalanche and the others detect the charge spread in the resistive foil.

To parametrize the PRF we used the ratio of two symmetric 4^{th} order polynoms proposed in [15]:

$$PRF(x, \Gamma, \Delta, a, b) = A \times \frac{1 + a_2 x^2 + a_4 x^4}{1 + b_2 x^2 + b_4 x^4} \tag{3}$$

where the parameters a_i and b_i can be related to the more physical parameters: the full width half maximum Γ, the base width Δ, and two scaling parameters a and b.

7.2. Spatial resolution estimation

To determine the PRF parameters, we initially use the track position reconstruction obtained from the barycentric method. After having defined the position of all the clusters, the global track is fit with a parabola. The fit is based on many measurements ($\geqslant 34$) thus it's considered as a true track position and the PRF scattered plot is filled (Figure 8 (a)). The scattered plot is profiled along Y axis to form a graph that is further fit with analytical function from Equation 3 (Figure 8 (b)).

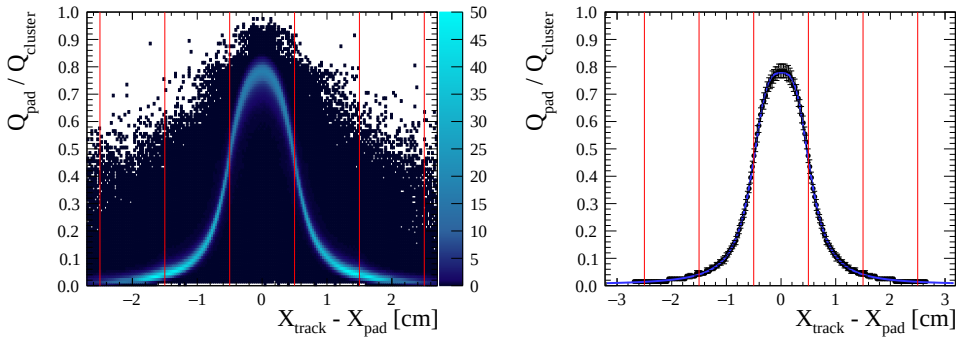

a b

Figure 8: The Pad Response Function (PRF) obtained with (a) scattered plot and (b) results of the profile and fit with analytical function. The pad borders are represented with vertical lines.

After having determined the PRF, the track position in each cluster is obtained with the following χ^2 minimization:

$$\chi^2 = \sum_{pads} \frac{Q_{pad}/Q_{cluster} - PRF\left(x_{track} - x_{pad}\right)}{\sigma_{Q_{pad}/Q_{cluster}}} \tag{4}$$

where σ_Q is the uncertainty on the charge measurements. In our analysis, we assume that charge measurement probability follows a Poisson distribution, hence: $\sigma_{Q_{pad}/Q_{cluster}} = \sqrt{Q_{pad}/Q_{cluster}}$. We proceed through the iterative process of the PRF estimation until the track fit quality is not improving anymore. Typically this procedure converges after X iterations.

The spatial resolution is defined as the difference between the reconstructed position in a given cluster and the global fit (residual). The particular cluster where the resolution is studied is excluded from the fit to prevent biases. The residuals distribution is fit with a Gaussian function whose standard deviation defines the spatial resolution.

7.3. Dependence on the drift distance, momentum, high voltage

The spatial resolution was studied over different samples. The beam position was varied within the drift distance of the field cage keeping the tracks parallel to the MicroMegas plane. The spatial resolution is expected to degrade slightly for a larger drift distance affected by the transverse and longitudinal diffusion. The observed dependence is shown in Figure 9 (a).

In addition, the high voltage applied to the MicroMegas mesh was varied to study the detector performance in different regimes. Higher voltage is expected to enhance the initial avalanche, thus increase the charge spreading signal. Signals in the neighbours pads are then more likely to pass the threshold and are less affected by statistical fluctuations. As track position reconstruction relies on the charge spreading measurements we expect a better performance with higher voltage. The results are shown in Figure 9 (b).

DESY beamline allow to tune the momentum of the electrons track to be delivered to the testbeam area. In this way we studied spatial resolution over the track kinematics. We find no significant changes for the position accuracy reconstruction for the tracks in range between 1 and 5 GeV/c (Figure 10).

7.4. Dependence on the track inclination

Inclined tracks are expected to be reconstructed less precisely compared to horizontal ones. As an example, in the current ND280 TPCs, the resolution

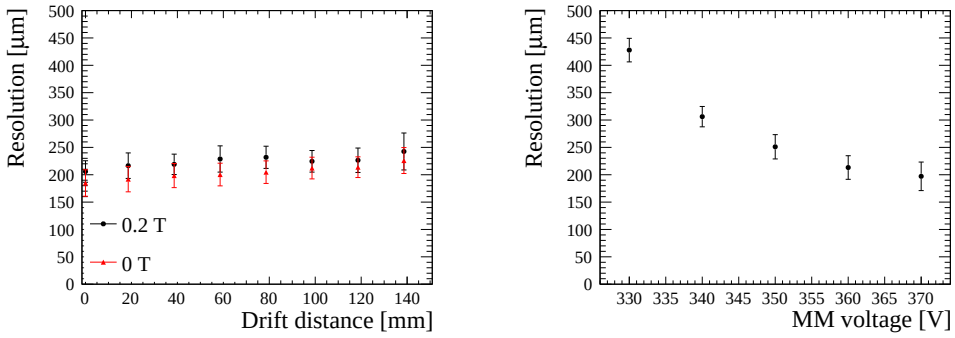

Figure 9: Spatial resolution w.r.t. (a) beam injection position and (b) MicroMegas voltage for horizontal tracks parallel to the MM plane. Points represent the mean value over detector columns and errors represent the fluctuations (RMS).

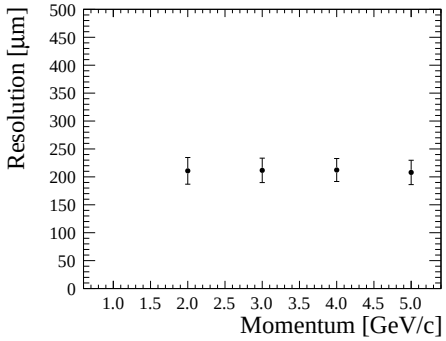

Figure 10: Spatial resolution over the momentum of the electron beam.

degrades as a function of the track angle from $600\mu m$ to $\sim 1\ mm$ [6]. It is then particularly interesting to investigate the behavior of the spatial resolution in the ERAM detector as a function of the track angle with respect to the ERAM plane.

In order to do this, the different cluster patterns described in section 5 were used for different track inclination. The χ^2 fit (Equation 4) is applied to each cluster to extract the track position. As for horizontal tracks, the positions in given clusters are fit together to form a global fit and the iterative analysis is applied: the barycentric estimation is used as a prior following with PRF calibration. The results of the inclined track spatial resolution

estimations are shown in Figure 11.

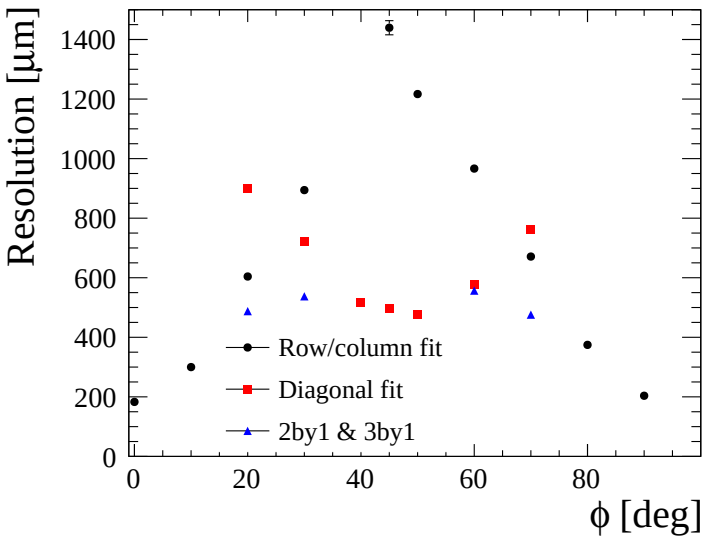

Figure 11: Spatial resolution w.r.t. track angle within the MM plane obtained with different cluster definitions.

As expected, the column clustering method leads to a severe spatial resolution degradation with the track slope, reaching a maximum of 1.4 mm for 45°tracks. For these angles, the diagonal pattern provides significant performance improvement. In the intermediate regions (20°, 30°, 60°, 70°), the best result is achieved with the more complex patterns: "2 by 1" and "3 by 1". The asymmetry w.r.t. 45° is caused by the rectangular pad shape 11.3×10.2 mm. Thus, the diagonal pattern is considered as a better choice for 48°tracks than for 45°tracks. Hence, tracks inclined with 50°are reconstructed more accurately compared to 40°tracks. Similar behaviour is observed for all the other patterns.

By taking the best clustering algorithm we observe a spatial resolution better than 600 μm for all the angles. We understand the difference between horizontal tracks and inclined tracks as due to the larger effective pad size for diagonal clustering and to the rectangular shape of the pads, while diagonal clustering would work better for square pads. For a spatial resolution of 600 μm, for 70 point measurements and a magnetic field of 0.2 T we expect a momentum resolution of 6% at 1 GeV/c that scales linearly with the spatial

resolution.

7.5. Bias measurements

As described above, we define the spatial resolution as a standard deviation of the difference between the reconstructed position in a given cluster and a global track fit. Meanwhile, the mean value of the residuals is also an important characteristic that shows the bias of our measurements. In particular, it's interesting to study the biases with respect to the track position in the pad. For that, we use the natural beam spread. The electron beam profile is nearly Gaussian with a standard deviation $\approx$ 1 cm. We sample the residuals with the reconstructed track position in the pad. Thus, we can study the resolution and biases in the different pad regions. In Figure 12, we show both the spatial resolution and bias per columns. Individual PRF were used for each column to analyse the behaviour in the different regions of the detector independently. The resolution undergoes some oscillations because if a track is close to one of the leading pad borders, the neighbouring pads see a larger signal and we thus have a more reliable input for the position reconstruction.

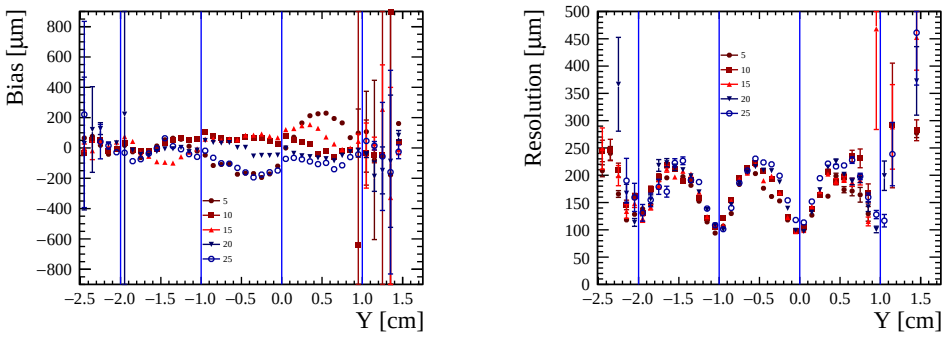

Figure 12: The resolution and the bias of the track reconstruction over the position in the pad for various columns. The pad borders are represented with vertical lines.

We generalise the bias study for the whole detector. Figure 13 represents the fluctuations of the resolution and biases in the given column. We conclude that for most of the detector the biases are under control and smaller comparing to the spatial resolution. In the downstream part of the detector, we found larger biases that could be related to the non-uniformities in the resistivity of this ERAM detector that will be described in section 9.

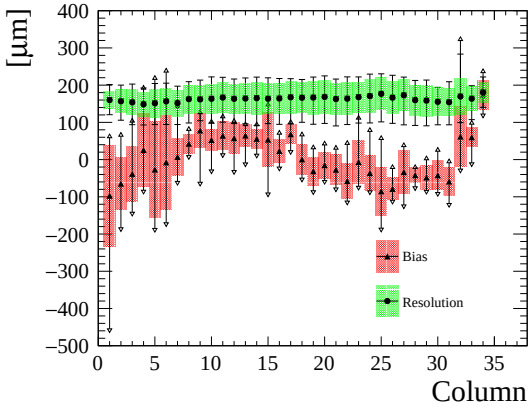

Figure 13: The spatial resolution and bias fluctuations observed for the different position of the track in the pad. Dots represent the mean value in a given column, filled areas correspond to the RMS, and error bars represent minimum and maximum values.

8. Deposited energy resolution

One of the main goals of a TPC is to perform particle identification (PID) based on the measurement of the ionization produced by charged particles crossing the gas volume. The PID capabilities depend on the resolution in the ionization measurements.

In case of T2K TPCs, the PID is mainly used to distinguish electrons (produced by ν_e) from muons (produced by ν_μ). In the momentum range studied by T2K, the amount of ionization between electrons and muons differs by $\sim 40\%$. Therefore, a resolution of less than 10% is needed to efficiently distinguish these two particles. In general, the resolution depends on the number of independent ionization measurements (i.e. the number of clusters) and on the amount of ionization in each cluster. For the existing TPCs, a resolution of 8% was obtained by combining measurements in 2 MicroMegas detectors (72 independent measurements of ionization).

In this section, we will describe the performances observed with one single ERAM detector (36×32 pads).

The method used to estimate the energy loss of a given track is called the truncated mean method: the charges contained in each cluster of the track are sorted by increasing order and only a fraction of lowest charges is kept to compute the mean deposited energy per track. Such a method allows to reject clusters with large amount of charge, due to fluctuations in

the ionization processes, that would degrades the resolution.

The dependence of the dE/dx resolution on the truncation fraction is shown in Figure 14. The best resolution is obtained for values of truncation fraction between 50% and 70%. Therefore, for all the results presented in this section, a truncation factor of 70% is used.

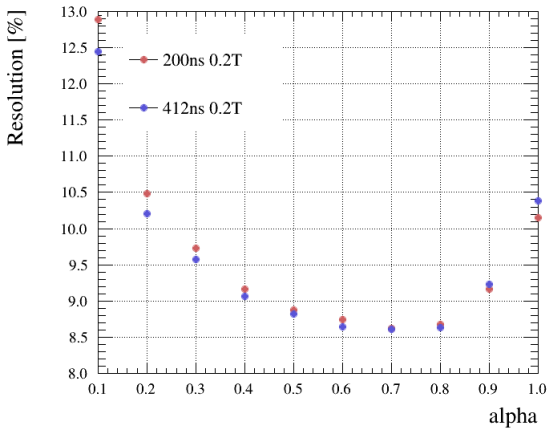

Figure 14: The dependence of the dE/dx resolution on the truncation factor α for the beam parallel to the pad plane with a magnetic field of 0.2 T and peaking times of either 200 ns and 412 ns

8.1. Definition of the cluster charge

As explained before, the basic ingredient of the dE/dx resolution is the amount of charge seen in each cluster. This quantity can be defined in different ways.

In the existing ND280 TPCs or in the results published in [7], the cluster charge is defined by summing the waveform maximum seen in each pad composing the cluster. This definition was shown to be a good estimator of the charge in the case of bulk MicroMegas, or when the drift distance is large enough to allow the predominance of transverse diffusion over the charge spreading induced in the ERAM module.

However, in the present configuration, the limited size of the TPC implies that the transverse diffusion is small and that charge spreading dominates. Therefore, by summing the maximum of the waveform seen in each pad of the cluster, we are double counting the leading pad charge: first it is seen

in the leading pad before the spread, and then seen by the neighboring pads after the spread.

To remove this double counting effect, the charge per cluster can be defined in a different way. For each cluster, we build a summed waveform defined as the sum of the waveform amplitude seen in each pad of the cluster at all times. We then take as a cluster charge estimator the maximum of this summed waveform. We refer to this method as WF_{sum}.

A comparison of the results of the two methods as a function of the drift distance is shown in Figure 15 for the two different peaking times and for data taken with 0.2 T magnetic field and with the beam parallel to the ERAM plane. It can be seen that with both methods, the resolution is well below 10% for all the drift distances and, as expected, the WF_{sum} method gives a better resolution comprised between 8.5% and 9.0%.

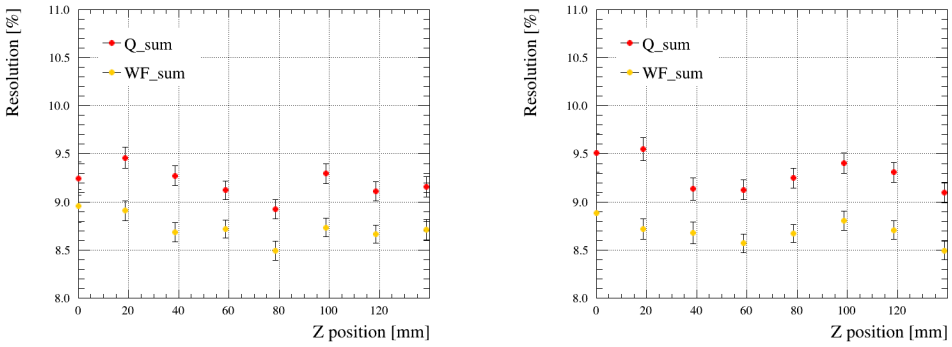

a b

Figure 15: dE/dx resolution with respect to the drift distance for the beam parallel to the pad plane with a magnetic field of 0.2 T and peaking times of 200 ns (a) and 412 ns (b). Q_{sum} method consists in summing the maximum of the waveform in each pad of the cluster while WF_{sum} corresponds to maximum of the summed waveforms in a cluster.

8.2. Deposited energy resolution for inclined tracks

As explained in section 5, in order to reconstruct inclined tracks, different clustering algorithms are used. In the case of the deposited energy resolution, the usage of such algorithms has two impacts: a larger number of clusters per track are reconstructed but the track will have different paths in different clusters.

In the column or row clusters, tracks with same angle with respect to the pad plane have the same dX in each cluster (neglecting the curvature

induced by the magnetic field). This is not true for diagonal clusters in which the dX can vary between 0 and the diagonal of the pad ($\sim 1.5\ cm$). The distribution of the charge as a function of dX for tracks inclined of 45 degrees with respect to the pad plane is shown in Figure 16. It is clear from this figure that there is a dependence, although this dependence is not linear as one would expect from the simple consideration that the deposited energy should be proportional to the path.

The non-linearity is due to the fact that each cluster sees not only the direct charge due to the primary ionization, but it also sees some charge due to the spread on the resistive plane and to the transverse diffusion in the gas.

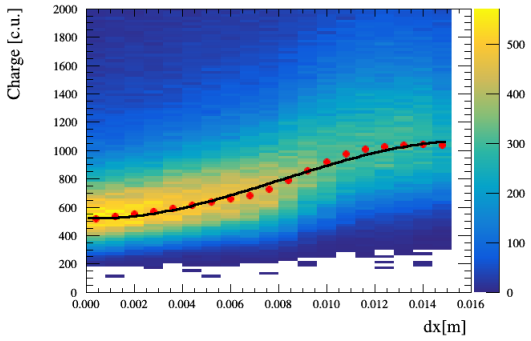

Figure 16: The distribution of the charge with respect to the dX of the track inclined of 45 degrees with respect to the pad plane

In order to correct the dX in each cluster, we fit the charge in each slice of dX with a Landau function and we take the Most Probable Value. The obtained distribution of MPV as a function of dX is then parametrized with a third degree polynomial. In each cluster, the charge is corrected to take into account the real path length dX and then the truncated mean is computed.

The dE/dx distributions for diagonal clustering with and without the dX correction are shown in Figure 17.

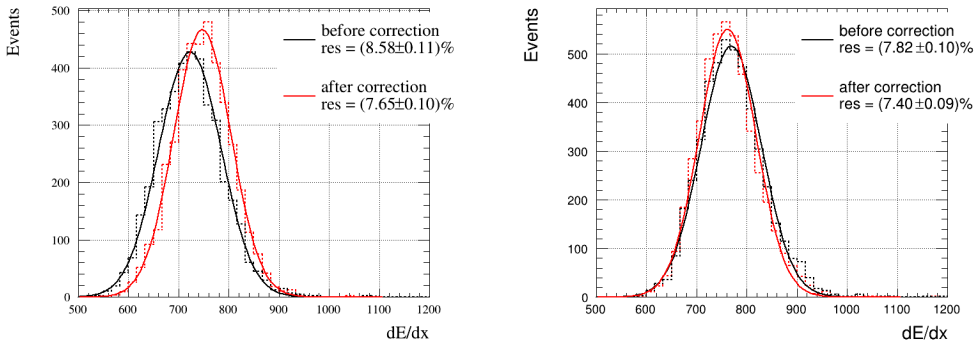

a b

Figure 17: The dE/dx distribution for 40 deg inclined tracks at a peaking time of 200 ns (a) and 412 ns (b) with and without the correction for dX.

The deposited energy resolution as a function of the beam inclination w.r.t. the pad plane is shown in Figure 18. As expected, the diagonal clustering, after proper dX correction, provides the best resolution thanks to the larger amount of clusters in which the track is sampled.

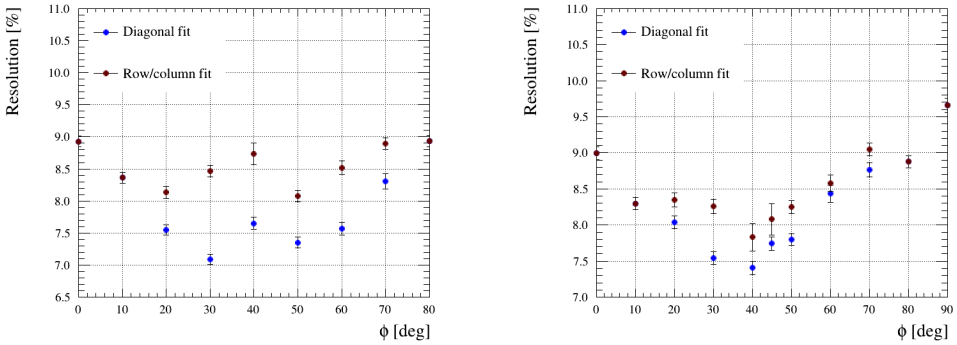

a b

Figure 18: dE/dx resolution versus the angle w.r.t pad plane using column/row clustering or diagonal clustering. Column clustering is used from 0 to 40 deg and after 40 deg row clustering is used. Runs at a peaking time of 200 ns (a) and 412 ns (b), with a magnetic field of 0.2T applied to the TPC prototype. Diagonal clustering are corrected for the dX as described in the text.

8.3. Dependence of the dE/dx resolution on the number of clusters

In this test beam, only one ERAM module was used. In the HA-TPC that will be installed at ND280, most of the tracks will cross two ERAM modules before exiting the TPC resulting in a larger number of clusters (72 for tracks parallel to the pad plane). The observed dependence of the deposited energy on the number of clusters can then be used to extrapolate the expected resolution in the HA-TPCs.

This can be done by computing the truncated mean using only a fraction of the available clusters. The dependence of the truncated mean on the number of clusters for different samples is shown in Figure 19.

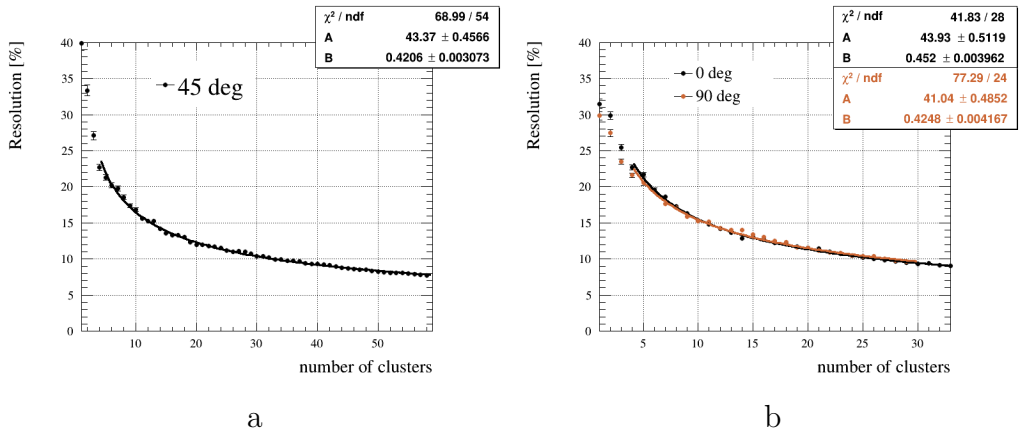

Figure 19: dE/dx resolution versus the number of clusters for runs at a peaking time of 412 ns with a magnetic field of 0.2T applied to the TPC prototype. Diagonal clustering (including dX correction) is used for 45 deg inclined tracks (a). In (b), column clustering is employed for 0 deg horizontal tracks and row clustering for 90 deg vertical tracks (b).

The resulting distribution of the deposited energy resolution as a function of the number of clusters N is then fit with the function: $f(N) = AN^{-B}$. B equal to 0.5 would correspond to a simple $\sqrt{N}$ dependence.

In the case of horizontal or vertical tracks, we observe similar behavior: the horizontal tracks being slightly better because of the larger pad size in the horizontal direction. Extrapolated to two ERAM modules, we obtain a deposited energy resolution of 5.42% using diagonal clustering.

9. RC map calculation

The quantity controlling the charge spreading over time is the product RC : R is the surface resistivity of the layer and C the capacitance determined by the spacing between the anode and readout planes. To have a better understanding of our detector, we reconstruct the map of RC using test beam data. This map is crucial to characterize our detector and its uniformity, and is also needed in the simulation. To extract these RC values, we use an analytical model of the charge dispersion, adjusted to the waveforms measured in the pads. The induced charge on a rectangular pad below the resistive layer can be calculated by integrating the charge density function over the pad area [16] :

$$\mathcal{Q}(t) = \frac{q_e}{4}\left[erf(\frac{x_{\text{high}} - x_0}{\sqrt{2}\sigma(t)}) - erf(\frac{x_{\text{low}} - x_0}{\sqrt{2}\sigma(t)})\right]\left[erf(\frac{y_{\text{high}} - y_0}{\sqrt{2}\sigma(t)}) - erf(\frac{y_{\text{low}} - y_0}{\sqrt{2}\sigma(t)})\right] \tag{5}$$

with q_e is the initial charge, (x_0,y_0) the track position, x_{high}, x_{low}, y_{high}, y_{low} the pad boundaries. In the denominator $\sigma(t) = \sqrt{(2t/\tau) + \omega^2}$, the term $\tau = RC$ where R is the surface resistivity of the layer and C the capacitance determined by the spacing between the anode and readout planes. Finally, ω is associated to the transverse diffusion term.

To compare to data, the characteristics of the front-end charge preamplifiers need also to be included. Longitudinal diffusion increases the size of electron charge clusters in the drift direction. The longitudinal diffusion is neglected here since we have only 15 cm drift distance. The parameterization of the electronics shaping time effects $\mathcal{I}(t)$ is obtained from the simulation. The convolution of $\mathcal{I}(t)$ and $\mathcal{Q}(t)$ results in the full theoretical model, which is compared to the data. This convolution is handled numerically. The fit is based on clusters of pads perpendicular to the track. Each cluster consists in a so-called leading pad collecting essentially the initial charge deposit, and in so-called neighbor pads sensitive mostly to the induced charge due to the resistive effect, as shown in Figure 4.

The fit procedure is as follows: we first fit the leading pad waveform with the electronics response function $\mathcal{I}(t)$, then we fit simultaneously the two

neighboring pads waveform with a convolution of $\mathcal{I}(t)$ with $\mathcal{Q}(t)$ in order to extract RC.

Then simultaneous fit of two neighboring pads waveform use separate $\mathcal{Q}(t)$ functions, as the distance to the track can be different for the two pads, but we consider RC and the electronics response parameters as common in the fit. Since we are using horizontal tracks, we can only fit the y_0-position of the track and we do not have any constraints on its x-position. The track position y_0 is obtained with the PRF χ^2 minimization method (see equation (4)). Figure 20 shows an example of waveform fit results for the leading pad and its neighbors.

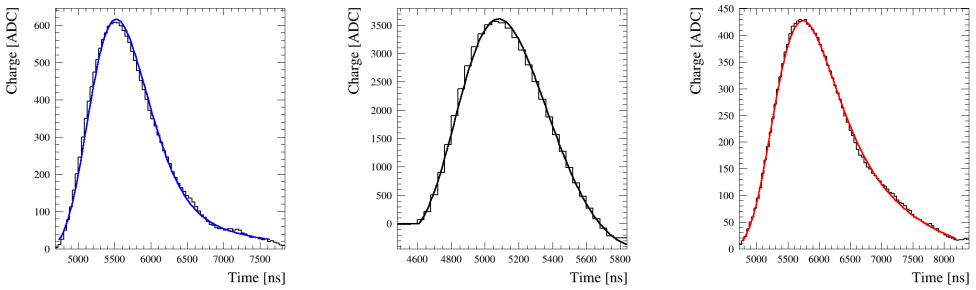

a b c

Figure 20: Example of waveform fit results for the leading pad (b) and its neighbors (a) and (c) in a given cluster.

Another method can be used to cross-check the RC values obtained with the analytical model. This alternative method studies two parameters related to the signal propagation: the time at which the signal in neighbour pads is maximal and the ratio of amplitudes of the neighbor pads and the leading pad. The time difference between the leading pad and one of its neighbor pad is found to be proportional to RC as can be seen in the following formula: $\Delta t_1 - \Delta t_2 = RC \times L \times y_0$, with L the pad length and y_0 the track position and $\Delta t_{1,2} = t_{\text{Leading Pad}} - t_{\text{Neighbor}}$ the time difference between the leading pad and the neighbor pad.

The RC maps obtained using the analytical model and the time difference method described above are shown in Figure 21. Both methods give results of the same order of magnitude though the second method is less precise than the fit procedure. A non-uniformity of RC up to 30% is observed using

both methods. This non-uniformity is confirmed with the observation of the charge collected in the second to leading pad. The charge observed in the leading pad is uniform across the detector while the measurements in the neighbours $Q_{\text{second}}/Q_{\text{leading}}$ demonstrate fluctuations, especially in the downstream detector region (Figure 22). Lower charge fraction is consistent with the higher RC value.

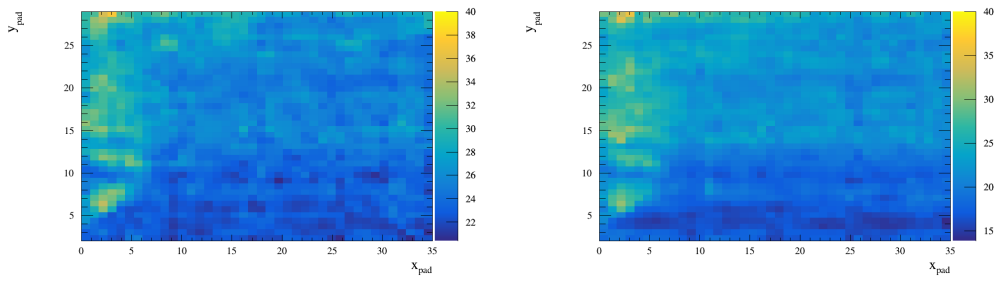

Figure 21: The RC map obtained using the fit from the analytical model (left) and the time difference method (right) described in the text.

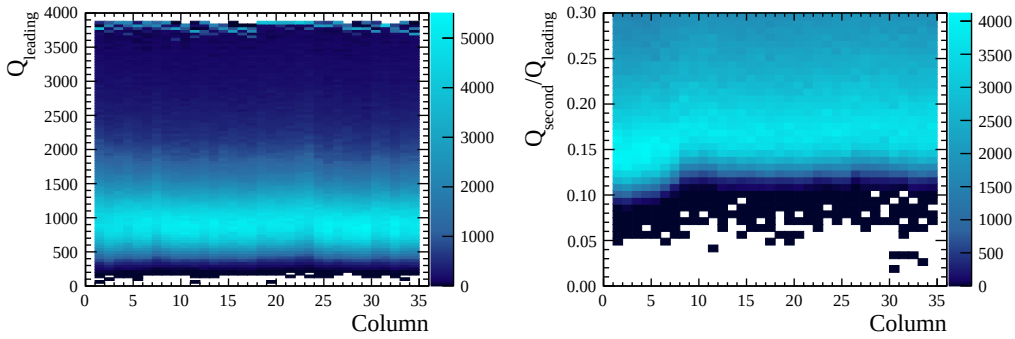

Figure 22: The distribution of the charge in the leading pad (left) and the charge fraction in the second to leading pad (right) versus the column for horizontal beam tracks.

10. Conclusions

Acknowledgements

The measurements leading to these results have been performed at the Test Beam Facility at DESY Hamburg (Germany), a member of the Helmholtz

Association.
The authors would like to thank the technical team at the DESY II accelerator and test beam facility for the smooth operation of the test beam and the support during the test beam campaign.

References

[1] K. Abe, et al., The T2K Experiment, Nucl. Instrum. Meth. A659 (2011) 106–135. arXiv:1106.1238, doi:10.1016/j.nima.2011.06.067.

[2] K. Abe, et al., Indication of Electron Neutrino Appearance from an Accelerator-produced Off-axis Muon Neutrino Beam, Phys. Rev. Lett. 107 (2011) 041801. arXiv:1106.2822, doi:10.1103/PhysRevLett.107.041801.

[3] K. Abe, et al., Evidence of Electron Neutrino Appearance in a Muon Neutrino Beam, Phys. Rev. D 88 (3) (2013) 032002. arXiv:1304.0841, doi:10.1103/PhysRevD.88.032002.

[4] K. Abe, et al., Observation of Electron Neutrino Appearance in a Muon Neutrino Beam, Phys. Rev. Lett. 112 (2014) 061802. arXiv:1311.4750, doi:10.1103/PhysRevLett.112.061802.

[5] K. Abe, et al., Constraint on the matter–antimatter symmetry-violating phase in neutrino oscillations, Nature 580 (7803) (2020) 339–344, [Erratum: Nature 583, E16 (2020)]. arXiv:1910.03887, doi:10.1038/s41586-020-2177-0.

[6] N. Abgrall, et al., Time Projection Chambers for the T2K Near Detectors, Nucl. Instrum. Meth. A637 (2011) 25–46. arXiv:1012.0865, doi:10.1016/j.nima.2011.02.036.

[7] D. Attié, et al., Performances of a resistive Micromegas module for the Time Projection Chambers of the T2K Near Detector upgrade, Nucl. Instrum. Meth. A 957 (2020) 163286. arXiv:1907.07060, doi:10.1016/j.nima.2019.163286.

[8] K. Abe, et al., T2K ND280 Upgrade - Technical Design Report (2019). arXiv:1901.03750.

[9] I. Giomataris, R. De Oliveira, S. Andriamonje, S. Aune, G. Charpak, P. Colas, A. Giganon, P. Rebourgeard, P. Salin, Micromegas in a bulk, Nucl. Instrum. Meth. A560 (2006) 405–408. arXiv:physics/0501003, doi:10.1016/j.nima.2005.12.222.

[10] M. S. Dixit, J. Dubeau, J. P. Martin, K. Sachs, Position sensing from charge dispersion in micropattern gas detectors with a resistive anode, Nucl. Instrum. Meth. A518 (2004) 721–727. arXiv:physics/0307152, doi:10.1016/j.nima.2003.09.051.

[11] R. Diener, et al., The DESY II Test Beam Facility, Nucl. Instrum. Meth. A 922 (2019) 265–286. arXiv:1807.09328, doi:10.1016/j.nima.2018.11.133.

[12] M. Ester, H.-P. Kriegel, J. Sander, X. Xu, A density-based algorithm for discovering clusters in large spatial databases with noise, in: Proceedings of the Second International Conference on Knowledge Discovery and Data Mining, AAAI Press, 1996, pp. 226–231.

[13] R. Gluckstern, Uncertainties in track momentum and direction, due to multiple scattering and measurement errors, Nuclear Instruments and Methods 24 (1963) 381–389. doi:https://doi.org/10.1016/0029-554X(63)90347-1.
URL https://www.sciencedirect.com/science/article/pii/0029554X63903471

[14] D. Attie, Beam tests of Micromegas LC-TPC large prototype, JINST 6 (2011) C01007. doi:10.1088/1748-0221/6/01/C01007.

[15] K. Boudjemline, M. S. Dixit, J. P. Martin, K. Sachs, Spatial resolution of a GEM readout TPC using the charge dispersion signal, Nucl. Instrum. Meth. A574 (2007) 22–27. arXiv:physics/0610232, doi:10.1016/j.nima.2007.01.017.

[16] M. S. Dixit, J. Dubeau, J. P. Martin, K. Sachs, Position sensing from charge dispersion in micropattern gas detectors with a resistive anode, Nucl. Instrum. Meth. A518 (2004) 721–727. arXiv:physics/0307152, doi:10.1016/j.nima.2003.09.051.